Research Article | Vol. 8, No. 12 | 1 Dec 2017 | BIOMEDICAL OPTICS EXPRESS 5637
Biomedical Optics EXPRESS

Optical projection tomography for rapid whole mouse brain imaging

DAVID NGUYEN,[1,*] PAUL J. MARCHAND,[1] ARIELLE L. PLANCHETTE,[1] JULIA NILSSON,[2] MIGUEL SISON,[1] JÉRÔME EXTERMANN,[1] ANTONIO LOPEZ,[1] MARCIN SYLWESTRZAK,[1] JESSICA SORDET-DESSIMOZ,[1] ANJA SCHMIDT-CHRISTENSEN,[2] DAN HOLMBERG,[2] DIMITRI VAN DE VILLE,[3] AND THEO LASSER[1]

[1]*Laboratoire d'Optique Biomédicale, School of Engineering, École Polytechnique Fédérale de Lausanne, CH-1015 Lausanne, Switzerland*
[2]*Autoimmunity, Department of Experimental Medical Sciences, Lund University Diabetes Centre, 20502 Malmö, Sweden*
[3]*Medical Image Processing Lab, School of Engineering, École Polytechnique Fédérale de Lausanne, CH-1202 Genève, Switzerland*
[*]*david.nguyen@epfl.ch*

Abstract: In recent years, three-dimensional mesoscopic imaging has gained significant importance in life sciences for fundamental studies at the whole-organ level. In this manuscript, we present an optical projection tomography (OPT) method designed for imaging of the intact mouse brain. The system features an isotropic resolution of ~50 μm and an acquisition time of four to eight minutes, using a 3-day optimized clearing protocol. Imaging of the brain autofluorescence in 3D reveals details of the neuroanatomy, while the use of fluorescent labels displays the vascular network and amyloid deposition in 5xFAD mice, an important model of Alzheimer's disease (AD). Finally, the OPT images are compared with histological slices.

OCIS codes: (110.0110) Imaging systems; (110.6880) Three-dimensional image acquisition; (110.6960) Tomography; (170.0170) Medical optics and biotechnology; (170.2520) Fluorescence microscopy;(180.0180) Microscopy; (180.6900) Three-dimensional microscopy.

References and links

1. V. Ntziachristos, "Going deeper than microscopy: the optical imaging frontier in biology," Nat. Methods **7**(8), 603–614 (2010).
2. A. Li, H. Gong, B. Zhang, Q. Wang, C. Yan, J. Wu, Q. Liu, S. Zeng, and Q. Luo, "Micro-optical sectioning tomography to obtain a high-resolution atlas of the mouse brain," Science **330**(6009), 1404–1408 (2010).
3. H. Gong, S. Zeng, C. Yan, X. Lv, Z. Yang, T. Xu, Z. Feng, W. Ding, X. Qi, A. Li, J. Wu, and Q. Luo, "Continuously tracing brain-wide long-distance axonal projections in mice at a one-micron voxel resolution," Neuroimage **74**, 87–98 (2013);
4. J. Huisken, and D. Y. R. Stainier, "Selective plane illumination microscopy techniques in developmental biology," Development **136**(12), 1963–1975 (2009).
5. B.-C. Chen, W. R. Legant, K. Wang, L. Shao, D. E. Milkie, M. W. Davidson, C. Janetopoulos, X. S. Wu, J. A. Hammer III, Z. Liu, B. P. English, Y. Mimori-Kiyosue, D. P. Romero, A. T. Ritter, J. Lippincott-Schwartz, L. Fritz-Laylin, R. D. Mullins, D. M. Mitchell, J. N. Bembenek, A.-C. Reymann, R. Böhme, S. W. Grill, J. T. Wang, G. Seydoux, U. S. Tulu, D. P. Kiehart, and E. Betzig, "Lattice light-sheet microscopy: imaging molecules to embryos at high spatiotemporal resolution," Science **346**(6208), 1257998 (2014).
6. A. Kaufmann, M. Mickoleit, M. Weber, and J. Huisken, "Multilayer mounting enables long-term imaging of zebrafish development in a light sheet microscope," Development **139**(17), 3242–3247 (2012).
7. P. J. Keller, A. D. Schmidt, A. Santella, K. Khairy, Z. Bao, J. Wittbrodt, and E. H. K. Stelzer, "Fast, high-contrast imaging of animal development with scanned light sheet-based structured-illumination microscopy," Nat. Methods **7**(8), 637–642 (2010).
8. H.-U. Dodt, U. Leischner, A. Schierloh, N. Jährling, C. P. Mauch, K. Deininger, J. M. Deussing, M. Eder, W. Zieglgänsberger, and K. Becker, "Ultramicroscopy: three-dimensional visualization of neuronal networks in the whole mouse brain," Nat. Methods **4**(4), 331–336 (2007).
9. L. Silvestri, A. L. A. Mascaro, I. Costantini, L. Sacconi, and F. S. Pavone, "Correlative two-photon and light sheet microscopy," Methods **66**, 268–272 (2014).

#301816 https://doi.org/10.1364/BOE.8.005637
Journal © 2017 Received 11 Jul 2017; revised 31 Oct 2017; accepted 31 Oct 2017; published 15 Nov 2017

Biomedical Optics EXPRESS

10. E. Lugo-Hernandez, A. Squire, N. Hagemann, A. Brenzel, M. Sardari, J. Schlechter, E. H. Sanchez-Mendoza, M. Gunzer, A. Faissner, and D. M. Hermann, "3D visualization and quantification of microvessels in the whole ischemic mouse brain using solvent-based clearing and light sheet microscopy," J. Cereb. Blood Flow Metab. **0**(00), 1–13 (2017).
11. N. Jährling, K. Becker, B. M. Wegenast-Braun, S. A. Grathwohl, M. Jucker, and H.-U. Dodt, "Cerebral β-amyloidosis in mice investigated by ultramicroscopy," PLoS One **10**(5), e0125418 (2015).
12. E. G. Reynaud, J. Peychl, J. Huisken, and P. Tomancak, "Guide to light-sheet microscopy for adventurous biologists," Nat. Methods **12**(1), 30–34 (2015).
13. J. Sharpe, U. Ahlgren, P. Perry, B. Hill, A. Ross, J. Hecksher-Sørensen, R. Baldock, and D. Davidson, "Optical projection tomography as a tool for 3D microscopy and gene expression studies," Science **296**(5567), 541–545 (2002).
14. A. C. Kak and M. Slaney, *Principles of Computerized Tomographic Imaging* (IEEE Press, 1988).
15. J. Sharpe, "Optical projection tomography as a new tool for studying embryo anatomy," J. Anat. **202**(2), 175–181 (2003).
16. M. D. Wong, J. Dazai, J. R. Walls, N. W. Gale, and R. M. Henkelman, "Design and Implementation of a custom built optical projection tomography system," PLoS One **8**(9), e73491 (2013).
17. A. Arranz, D. Dong, S. Zhu, M. Rudin, C. Tsatsanis, J. Tian, and J. Ripoll, "Helical optical projection tomography," Opt. Express **21**(22), 25912–25925 (2013).
18. J. R. Walls, J. G. Sled, J. Sharpe, and R. M. Henkelman, "Correction of artefacts in optical projection tomography," Phys. Med. Biol. **50**(19), 4645–4665 (2005).
19. J. R. Walls, J. G. Sled, J. Sharpe, and R. M. Henkelman, "Resolution improvement in emission optical projection tomography," Phys. Med. Biol. **52**(10), 2775–2790 (2007).
20. D. Dong, S. Zhu, C. Qin, V. Kumar, J. V. Stein, S. Oehler, C. Savakis, J. Tian, and J. Ripoll, "Automated recovery of the center of rotation in optical projection tomography in the presence of scattering," IEEE J. Biomed. Health Inform. **17**(1), 198–204 (2013).
21. C. Vinegoni, D. Razansky, J.-L. Figueiredo, M. Nahrendorf, V. Ntziachristos, and R. Weissleder, "Normalized Born ratio for fluorescence optical projection tomography," Opt. Lett. **34**(3), 319–321 (2009).
22. T. Correia, N. Lockwood, S. Kumar, J. Yin, M.-C. Ramel, N. Andrews, M. Katan, L. Bugeon, M. J. Dallman, J. McGinty, P. Frankel, P. M. W. French, and S. Arridge, "Accelerated optical projection tomography applied to in vivo imaging of zebrafish," PLoS One **10**(8), e0136213 (2015).
23. C. Vinegoni, L. Fexon, P. F. Feruglio, M. Pivovarov, J.-L. Figueiredo, M. Nahrendorf, A. Pozzo, A. Sbarbati, and R. Weissleder, "High throughput transmission optical projection tomography using low cost graphics processing unit," Opt. Express **17**(25), 22320–22332 (2009).
24. A. Bassi, L. Fieramonti, C. D'Andrea, M. Mione, and G. Valentini, "In vivo label-free three-dimensional imaging of zebrafish vasculature with optical projection tomography," J. Biomed. Opt. **16**(10), 100502 (2011).
25. A. Arranz, D. Dong, S. Zhu, C. Savakis, J. Tian, and J. Ripoll, "In-vivo optical tomography of small scattering specimens: time-lapse 3D imaging of the head eversion process in Drosophila melanogaster," Sci. Rep. **4**, 7325 (2014).
26. C. Vinegoni, C. Pitsouli, D. Razansky, N. Perrimon, and V. Ntziachristos, "In vivo imaging of Drosophila melanogaster pupae with mesoscopic fluorescence tomography," Nat. Methods **5**(1), 45–47 (2008).
27. J. McGinty, H. B. Taylor, L. Chen, L. Bugeon, J. R. Lamb, M. J. Dallman, and P. M. W. French, "In vivo fluorescence lifetime optical projection tomography," Biomed. Opt. Express **2**(5), 1340–1350 (2011).
28. K. Lee, J. Avondo, H. Morrison, L. Blot, M. Stark, J. Sharpe, A. Bangham, and E. Coen, "Visualizing plant development and gene expression in three dimensions using optical projection tomography," Plant Cell **18**(9), 2145–2156 (2006).
29. K. J. I. Lee, G. M. Calder, C. R. Hindle, J. L. Newman, S. N. Robinson, J. J. H. Y. Avondo, and E. S. Coen, "Macro optical projection tomography for large scale 3D imaging of plant structures and gene activity," J. Exp. Bot. **68**(3), 527–538 (2016).
30. T. Alanentalo, C. E. Lorén, Å. Larefalk, J. Sharpe, D. Holmberg, and U. Ahlgren, "High-resolution three-dimensional imaging of islet- infiltrate interactions based on optical projection tomography assessments of the intact adult mouse pancreas," J. Biomed. Opt. **13**(5), 054070 (2008).
31. T. Alanentalo, A. Hörnblad, S. Mayans, A. K. Nilsson, J. Sharpe, Å. Larefalk, U. Ahlgren, and D. Holmberg, "Quantification and three-dimensional imaging of the insulitis-induced destruction of β-cells in murine type 1 diabetes," Diabetes **59**(7), 1756–1764 (2010).
32. S. Gupta, R. Utoft, H. Hasseldam, A. Schmidt-Christensen, T. D. Hannibal, L. Hansen, N. Fransén-Pettersson, N. Agarwal-Gupta, B. Rozell, Â. Andersson, and D. Holmberg, "Global and 3D spatial assessment of neuroinflammation in rodent models of multiple sclerosis," PLoS One **8**(10), e76330 (2013).
33. J. A. Gleave, M. D. Wong, J. Dazai, M. Altaf, R. M. Henkelman, J. P. Lerch, and B. J. Nieman, "Neuroanatomical phenotyping of the mouse brain with three-dimensional autofluorescence imaging," Physiol. Genomics **44**(15), 778–785 (2012).
34. J. A. Gleave, J. P. Lerch, R. M. Henkelman, and B. J. Nieman, "A method for 3D immunostaining and optical imaging of the mouse brain demonstrated in neural progenitor cells," PLoS One **8**(8), e72039 (2013).
35. H. Oakley, S. L. Cole, S. Logan, E. Maus, P. Shao, J. Craft, A. Guillozet-Bongaarts, M. Ohno, J. Disterhoft, L. Van

Biomedical Optics EXPRESS

Eldik, R. Berry, and R. Vassaar, "Intraneuronal beta-amyloid aggregates, neurodegeneration, and neuron loss in transgenic mice with five familial Alzheimer's disease mutations: potential factors in amyloid plaque formation," J. Neurosci. **26**(40), 10129–10140 (2006).
36. S. Inoué and K. R. Spring, *Video Microscopy - The Fundamentals* (Springer US, 1997).
37. J. Schindelin, I. Arganda-Carreras, E. Frise, V. Kaynig, M. Longair, T. Pietzsch, S. Preibisch, C. Rueden, S. Saalfeld, B. Schmid, J.-Y. Tinevez, D. J. White, V. Hartenstein, K. Eliceiri, P. Tomancak, and A. Cardona, "Fiji: an open-source platform for biological-image analysis," Nat. Methods **9**(7), 676–682 (2012).
38. P. Thévenaz and M. Unser, "User-friendly semiautomated assembly of accurate image mosaics in microscopy," Microsc. Res. Tech. **70**(2), 135–146 (2006).
39. M.-T. Ke, S. Fujimoto, and T. Imai, "SeeDB: a simple and morphology-preserving optical clearing agent for neuronal circuit reconstruction," Nat. Neurosci. **16**, 1154–1161 (2013).
40. J. R. Walls, L. Coultas, J. Rossant, and R. M. Henkelman, "Three-dimensional analysis of vascular development in the mouse embryo," PLoS One **3**(8), e2853 (2008).
41. E. S. Lein, *et al.*, "Genome-wide atlas of gene expression in the adult mouse brain," Nature **445**, 168–176 (2007).
42. K. Chung, and K. Deisseroth, "CLARITY for mapping the nervous system," Nat. Methods **10**, 508–513 (2013).
43. H. Hama, H. Kurokawa, H. Kawano, R. Ando, T. Shimogori, H. Noda, K. Fukami, A. Sakaue-Sawano, and A. Miyawaki, "Sca*l*e: a chemical approach for fluorescence imaging and reconstruction of transparent mouse brain," Nat. Neurosci. **14**, 1481–1488 (2011).
44. A. Ertürk, K. Becker, N. Jährling, C. P. Mauch, C. D. Hojer, J. G. Egen, F. Hellal, F. Bradke, M. Sheng, and H.-U. Dodt, "Three-dimensional imaging of solvent-cleared organs using 3DISCO," Nat. Protoc. **7**, 1983–1995 (2012).

1. Introduction

Since its invention in the 19th century, histopathology has been and continues to be a widely used method for tissue-based medical diagnosis. While it excels at producing two-dimensional images of tissue sections, extracting information from whole three-dimensional tissues remains challenging. As a complement to histopathology, a new imaging regime, termed mesoscopy [1] emerged at the beginning of the century for 3D visualization of samples spanning a scale from a few millimeters to several centimeters. Over time, various techniques have been developed within this regime.

Micro-optical sectioning tomography (MOST) [2] is a block-face imaging method where the process of histology is automatized via simultaneous imaging and sectioning of the tissue. This technique has been successfully applied to image a whole mouse brain with a submicrometric resolution [3]. However, the acquisition time of approximately two weeks represents an experimental limitation for studies involving numerous animals.

Light-sheet microscopy [4] is probably the most prolific example of these mesoscopic techniques. Light-sheet microscopy performs three-dimensional imaging by scanning an engineered sheet of light orthogonal to the optical axis. This illumination mechanism achieves optical sectioning without slicing the tissue along with minimal photobleaching. The penetration depth of light-sheet microscopy is enhanced in naturally-transparent or cleared samples due to the reduction in light scattering. Recent research on light-sheet microscopy has mainly been focused on *in vivo* imaging. Improved illumination strategies (for example with optical lattices [5]), and solutions for specimen mounting in a physiological environment [6] have been developed. Additionally, the combination of light-sheet microscopy with structured illumination microscopy has increased the visibility through opaque samples [7], thus avoiding optical clearing (a process often done *ex vivo* due to its toxicity). Efforts have also been directed towards imaging larger samples, such as entire neural [8] and vascular networks [9, 10], or Alzheimer's disease (AD) hallmark amyloid deposition [11] in whole mouse brains. These particular results have helped to establish light-sheet microscopy as a tool for mouse phenotyping and investigations of disease models. Light-sheet microscopy produces outstanding 3D image quality with subcellular resolution over large volumes, which typically translates into big data sets. These require excessively long image processing time and terabytes of data handling [12]. Moreover, the optical design and image processing pipeline of such systems can be complex for inexperienced users. For these reasons, we propose optical projection tomography (OPT) as an alternative.

Biomedical Optics EXPRESS

OPT is a three-dimensional imaging technique developed by James Sharpe in 2002 [13] for 3D microscopy and gene expression studies. Considered as an optical analogue of X-ray computed tomography (CT) [14], OPT allows sample reconstruction from projections acquired at different angles. These projections are images taken over 360°, by rotating the sample, with a depth of field (DOF) covering half the specimen. Depending on the illumination, the projections either provide information on the light absorption or the integration of a fluorescence signal through the sample [15]. In both cases, the reconstruction of inner structures strongly depends upon the sample's transparency. For enhanced penetration depths, OPT requires naturally-transparent or cleared samples. Recently, custom OPT systems have been developed [16], including helical OPT [17], where a vertical translation is introduced during the acquisition process to enable imaging of elongated samples, such as rodent spinal cords and large intestines. Along with these hardware improvements, OPT benefited from several artifact-correction [18] and resolution improvement [19] algorithms. For example, to automatically recover the center of rotation (COR) in the projections [20] or to account for fluorescence absorption in tissues with a normalized Born approach [21]. Additionally, accelerated reconstruction procedures have been achieved by taking advantage of either iterative algorithms [22], or parallel processing on the graphics processing unit (GPU) [23]. Various applications highlight the performance of OPT. These include *in vivo* imaging of the zebrafish vasculature [24], fruit fly pupae head eversion process [25], morphogenesis of salivary glands and wing imaginal discs [26], as well as fluorescence lifetime in living zebrafish embryos [27], and visualization of plant development [28, 29]. Furthermore, OPT has been used for whole organ imaging in mice to study the pancreas and beta-cell tissue in the development of diabetes [30, 31], the spinal cord and optic nerve in the development of experimental autoimmune encephalomyelitis (EAE) [32], and to perform neuroanatomical phenotyping [33, 34]. So far, OPT is limited in resolution by the depth of field required for imaging. However, its rapidity and simplicity in image acquisition and processing make OPT convenient for various routine applications.

In this paper, we present a novel OPT methodology for whole mouse brain imaging. It includes an OPT design which uses the principle of epifluorescence, a feature known to maximize the rejection of stray light and homogenize the illumination in the sample plane. In addition to the setup design, we provide an outline of the software processing and demonstrate 3D imaging of the brain with an optimized solvent-based clearing protocol. A dehydration step of a single day in 100 % methanol with one refresh in the clearing protocol is shown to be sufficient to reveal details of the mouse neuroanatomy (while several days and increasing concentration of solvent solution were previously required [8, 11, 33]). Furthermore, our sample preparation has been successfully combined with different standard labeling protocols from fluorescence imaging technology to image the vasculature of wild-type mouse brains as well as the distribution of amyloid plaques in the brain of transgenic mice that coexpress five familial AD mutations (5xFAD mice) [35], an important model of the disease. Finally, we show a comparison of the OPT images with histological slices from the same mouse brain.

2. Materials and methods

2.1. Optical projection tomography

Our mesoscopic OPT setup (Fig. 1) is designed for 3D imaging of whole intact mouse brains. As shown in blue in Fig. 1(A) and 1(B), the detection arm consists of a 4f system with an objective lens L_o (f = 300 mm, AC508-300-A-ML, Thorlabs) and a tube lens L_t (f = 150 mm, AC508-150-A-ML, Thorlabs), both achromatic. This configuration results in a 0.5X magnification on the detector (ORCA-Flash 4.0 V2, Hamamatsu), providing a field of view (FOV) of 26.6×26.6 mm^2 over 1024×1024 px^2 in a 2×2 binning mode (initially 2048×2048 px^2). A DOF of approximately 15 mm (according to the definition of Inoué and Spring [36], equation 2.18) is obtained by placing a 4 mm diameter diaphragm in the rear focal plane of the objective lens, which also makes the

Biomedical Optics EXPRESS

system telecentric. The resulting numerical aperture (NA) of 0.01 provides a diffraction-limited lateral resolution of 28 µm (according to the definition of Inoué and Spring [36], equation 2.7). However, this diffraction-limited lateral resolution is currently hindered by the pixel-limited resolution of 52 µm (twice the binned pixel size). The projections are captured at angular steps of 0.3° (or 0.9° in Fig. 6(E)) by rotating the sample over 360° i.e., 1200 projections (or 400 projections in Fig. 6(E)), in a step-and-shoot mode. The reconstruction of samples as thick as 26 mm (limited by the FOV) is typically achieved within minutes (see Table 1 for details on exposure and acquisition time). As illustrated in green in Fig. 1(A), the sample is illuminated by switchable LEDs. In this manuscript, we use a 420 nm LED (M420D2, Thorlabs) and a 470 nm LED (M470D2, Thorlabs), also described in Table 1. These LEDs are collimated by an aspheric lens L_c (f = 16 mm, ACL25416U, Thorlabs). The resulting illumination beam is magnified by another 4f system composed of an achromatic relay lens L_r (f = 150 mm, AC254-150-A-ML, Thorlabs) and the objective lens, providing a uniform full-field illumination of the sample plane while maximizing the rejection of stray light. A kinematic fluorescence filter cube (DFM1/M, Thorlabs) is used to introduce and filter the illumination beam in the detection path (epifluorescence), and a modular LED switching mechanism (Fig. 1(C)) allows the user to choose between different fluorescence configurations (described in Table 1).

Table 1. OPT configuration to visualize different features of interest. Stated are LEDs, filters, exposure time, and total acquisition time. Filters references are from Chroma: EX, excitation filter; DC, dichroic mirror; EM, emission filter.

Feature *(marker)*	**Figure**	**LED**	**Filters**	**Exposure time** [s]	**Acquisition time** [min]
neuroanatomy *(autofluorescence)*	3	420 nm	EX, AT420/40x DC, AT455dc EM, AT465lp	0.2	4
vascular network *(FITC-albumin hydrogel)*	4, 6(B)-(C)	470 nm	EX, AT480/30x DC, AT505dc EM, AT535/40m	0.2-0.4	4-8
amyloid plaques *(Methoxy-X04)*	5, 6(E)	420 nm	EX, AT420/40x DC, AT455dc EM, AT465lp	0.15-0.3	3-6

Before imaging, the sample embedded in agarose is glued (Loctite 454, Loctite) on a holder and attached to a motorized rotation stage (8MR190-2, Standa) using a magnet, as depicted in Fig. 1(D). The OPT imaging takes place across a cuvette (704-001-30-10, Hellma Analytics) filled with a 1:2 mixture of benzyl alcohol and benzyl benzoate (BABB) for index matching. Three motorized linear stages (8MT167-100, Standa) provide additional degrees of freedom for aligning and focusing the sample. We use the translation along the y-axis to align the rotation axis on the center of the detector, and the magnet to align the sample gravity center on the rotation axis. These alignment procedures are necessary to keep the sample within the FOV of the setup but can be carried out approximately since the COR is numerically retrieved in the reconstruction algorithm. The tilt of the rotation axis has been minimized by precisely manufacturing the custom components and does not significantly affect the reconstruction process. More control on this parameter can be achieved by adding a tip-tilt mount on the rotation stage and using the alignment protocol described by Wong *et al.* [16].

2.2. Image processing

As illustrated in Fig. 2, image acquisition with the OPT system produces a stack of 1200 or 400 projections, separated by the same angular distance and depicting the sample over 360°.

Biomedical Optics EXPRESS

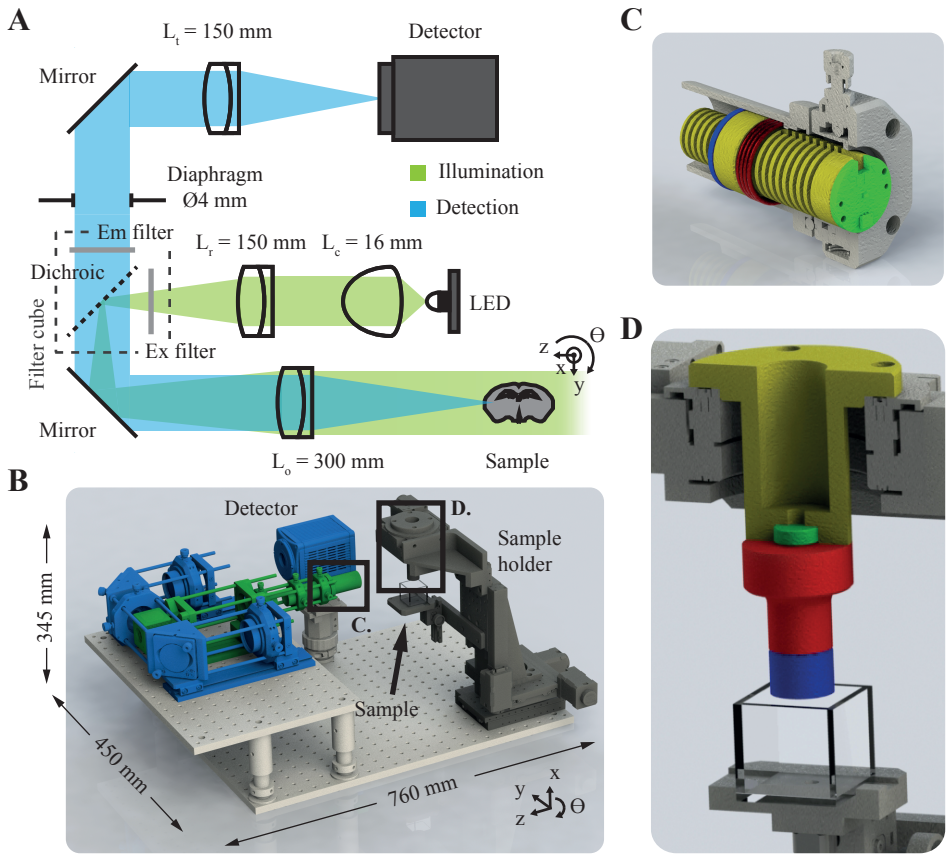

Fig. 1. OPT design. The optical layout (A) and the corresponding CAD rendering (B) illustrate the detection (blue) and illumination (green) arms. A detailed view of the LEDs mount (C) demonstrates the system for alignment and switching. It is composed of a custom heat sink (yellow), a spring (red, C.254.250.0250.A, Vanel), and a ring (blue, SM1RR, Thorlabs) stacked inside a 1-inch tube (SM1L20, Thorlabs) and screwed to a quick-release translation mount (CXY1Q, Thorlabs). The custom sample holding mechanism (D) consists of a base tube (yellow) glued to a magnet (green) to hold the magnetic stainless steel cylinder (red). The sample is glued to the blue cylinder which can be screwed to the whole mechanism.

These projections are pre-processed with Fiji [37] depending on the sample preparation. Brain autofluorescence reconstructions sometimes present ring artifacts [18], presumably due to a variation in the pixels response of the camera. A median filter (3 × 3, radius 0.5 px) is applied to the projections to mitigate this effect. Vasculature-labeled brain reconstructions display an increased contrast by applying a mean filter of the same size to the projections. No pre-processing step is applied to amyloid-labeled brain projections. A line is fit on the maximum values of the convolution of the first projection $I_{0°}$ with the opposite projection $I_{180°}$ along the vertical direction. This line forms a vector containing the CORs (shown with a green dotted line in Fig. 2), for each vertical position in the projection stack. These COR values are crucial to avoid artifacts in the reconstruction. The projection stack is transformed into a sinograms stack, by permuting the dimensions of the stack, and each sinogram is high-pass filtered with a Shepp-Logan filter. A 3D image of the sample is obtained by back-projecting each sinogram around the corresponding COR value with a linear interpolation. The sinograms' filtering and back-projection compose

Biomedical Optics EXPRESS

the conventional filtered back-projection (FBP) algorithm [14] and are implemented in CUDA (Nvidia) to take advantage of massive parallelization on the GPU. A desktop computer operated with Windows 7 Enterprise SP1 64-bit (Microsoft) and equipped with two Xeon CPU E5-2650 v2 (Intel), 64 GB DDR3 RAM, a GeForce GTX TITAN Black embedding 2880 CUDA cores, and 6 GB GDDR5 memory allows processing the samples in approximately 2 minutes for a resulting 8-bits stack of 1024 x 1024 x 1024 px^3 (around 0.5 GB in size). Finally, three-dimensional image rendering is performed with the Imaris (Bitplane) software.

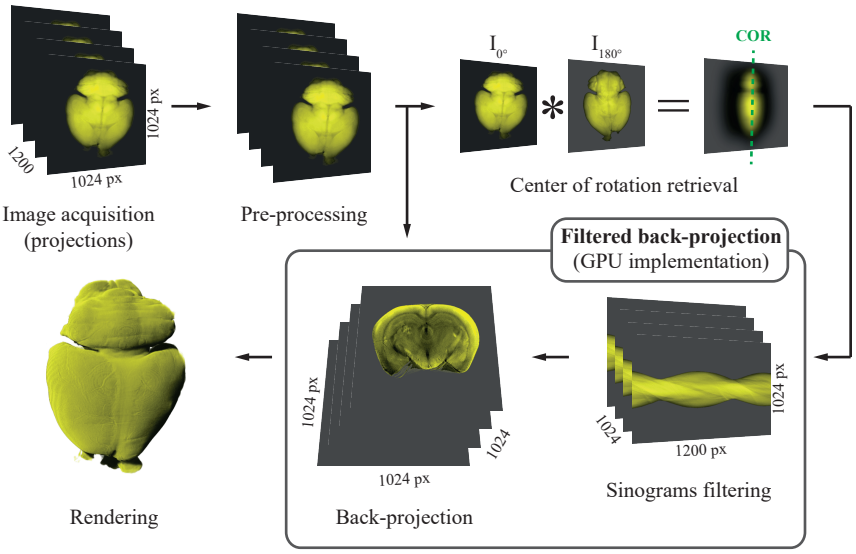

Fig. 2. Image processing pipeline illustrating the filtered back-projection (FBP) as well as the automatic retrieval of the COR algorithms. After a pre-processing step (described in text), the sinograms are filtered and the corresponding COR is retrieved. Following these operations, the sinograms are back-projected to form the virtual tissue sections, and 3D rendering is applied.

2.3. Mouse model

5xFAD genetically-modified mice [35] were purchased from The Jackson Laboratory on a congenic C57BL/6J background (34848-JAX, MMRRC). They were bred and maintained in-house with SJL/J mice (000686, The Jackson Laboratory) to generate the experimental animals on a hybrid B6SJL F1 background, which demonstrates a more robust amyloid phenotype. This model of AD is extensively used in research and displays many of the phenotypes associated with the disease [35]. In particular, the mice are known to develop an early and severe amyloid deposition starting from 1.5 months of age [35].

2.4. Sample preparation

All animal procedures were carried out according to Swiss regulations under the approval of the veterinary authority of the canton of Vaud.

Amyloid plaques labeling. Similar to the protocol reported by Jährling *et al.* [11], 5xFAD mice and their littermate controls, on a B6SJL F1 background, received two consecutive intraperitoneal (IP) injections of 30 mg/kg Methoxy-X04 (Tocris) in DMSO (10 mg/ml) with a 24-h interval. During the second injection, 100 µl (30 µg/ml) buprenorphine in 0.9 % NaCl was also administered subcutaneously (SC) for analgesia. Two hours later, the animals were deeply anesthetized IP with

Biomedical Optics EXPRESS

sodium pentobarbital (150 mg/kg) in aqueous solution (150 mg/ml). Once the depth of anesthesia was sufficient (assessed with toe pinch reflex), the animals were transcardially perfused with 2 ml of heparinized (5 I.U./ml) 1X PBS (pH 7.4), followed by 15 ml of 10 % formalin solution (HT501128, Sigma), at 4° C and 1.5 ml/min, for tissue fixation. After the perfusion, the brains were extracted and postfixed in 40 ml of formalin at 4° C overnight.

Vasculature labeling. B6SJL F1 mice were anesthetized as described above (including the injection of buprenorphine). Subsequently, an identical transcardial perfusion was performed with the additional 10 ml of hydrogel [10] at 40° C and 1.5 ml/min. The hydrogel is a mixture of 2 % (w/v) gelatin (G1890, Sigma) in 1X PBS (prepared at 60° C) and 0.1 % (w/v) FITC-conjugated albumin (A9771, Sigma) done at 40° C (0.22 µm-filtered). Before organ harvesting and fixation (as described above), the mouse head was incubated in ice-cold water for 10 minutes to solidify the hydrogel.

Organ clearing. After fixation, the organs were mounted in 1.5 % (w/v) agarose (16500500, Invitrogen) at 45° C with Milli-Q water (0.22 µm-filtered and degassed) and dehydrated in 40 ml of 100 % methanol (ME03161000, Scharlau) on a rotator (10 RPM) for 24 h with a renewal of the methanol after 15 h. Similar results (not shown here) were obtained by dehydration in ethanol. Then, the organs were transferred to a 40 ml solution of BABB (148390010 and 105860010, ACROS Organics) for optical clearing. This process can last for several days, but after approximately 48 h, the brain transparency is sufficient for imaging.

Histology. After fixation, the brains were split into hemispheres. One hemisphere was cleared and imaged with OPT. The other hemisphere was transferred to a 40 ml solution (0.22 µm-filtered) of 30 % (w/v) sucrose in 1X PBS (pH 7.4) at 4° C for approximately 48 h, or until the sample sunk at the bottom of the tube. Then the sample was partially dried on a tissue, placed in an embedding mold (such as 27112, Ted Pella Inc), and immersed in Cryomatrix (6769006, Thermo Scientific). Following the immersion in Cryomatrix, the mold was dipped in a bath of isopentane (avoid contact between Cryomatrix and isopentane) and dry ice until the Cryomatrix became completely opaque. Afterwards, the samples were stored at -80° C before slicing, with a sliding microtome, and mounting. The hemisphere sections were imaged on an Apotome (Zeiss) with a 5X, 0.15 NA air-objective, as well as a DAPI and wtGFP filter sets (for plaques and vasculature respectively). The Fiji plugin MosaicJ [38] was used to stitch the Apotome images together and create an image of the whole section.

3. Results and discussion

3.1. Neuroanatomy

To demonstrate the performance of our novel OPT approach, we started by clearing 2- to 8-month-old B6SJL F1 mouse brains (n>5). Figure 3(A) shows a representative image of a cleared brain at the age of 8 months. The transparency is sufficient to *see through* the organ and is adequate for OPT imaging (see Fig. 3(B) and 3(C)). Standard BABB clearing techniques require tissue immersion in increasing series of methanol concentration for dehydration to prevent cellular distortions and excessive shrinkage of the tissue. However, we found that it is not needed for OPT as the agarose embedding acts as a protective coating. The samples are directly dehydrated in 100 % methanol, and this simplifies the clearing protocol. Although not shown in Fig. 3, we observed shrinkage of the organs, a known side-effect of BABB clearing [39].

Images of the same 8-month-old brain were further acquired using the OPT system with the 420-nm excitation illumination, and a 3D rendering is shown in Fig. 3(B). With its 0.5X magnification and 15-mm DOF, the setup successfully captures the whole three-dimensional nature of the organ. Individual coronal sections (Fig. 3(C)) reveal details of the neuroanatomy down to the deepest structures. For example, the lateral (vl) and third (v3) ventricles are cavities in the brain, which get filled with BABB and therefore appear as dark regions in the sections. The caudoputamen (cp), identified through its sponge-like structure, and the thalamus (th), appear

Biomedical Optics EXPRESS

brighter. More brain regions can be identified via the different autofluorescence contrasts, such as the cortex (ctx), culmen (cul), and medial mammillary nucleus (mm), which present a higher contrast, the optic chiasms (och), which appear as a bright tube with a dark, presumably hollow, core, but also the corpus callosum (cc), the hippocampal region (hip), the inferior colliculus (ic), and the central lobule (cent). The identification of these different brain regions using the autofluorescence contrast confirms the ability of our OPT system to perform neuroanatomical phenotyping as described previously [33].

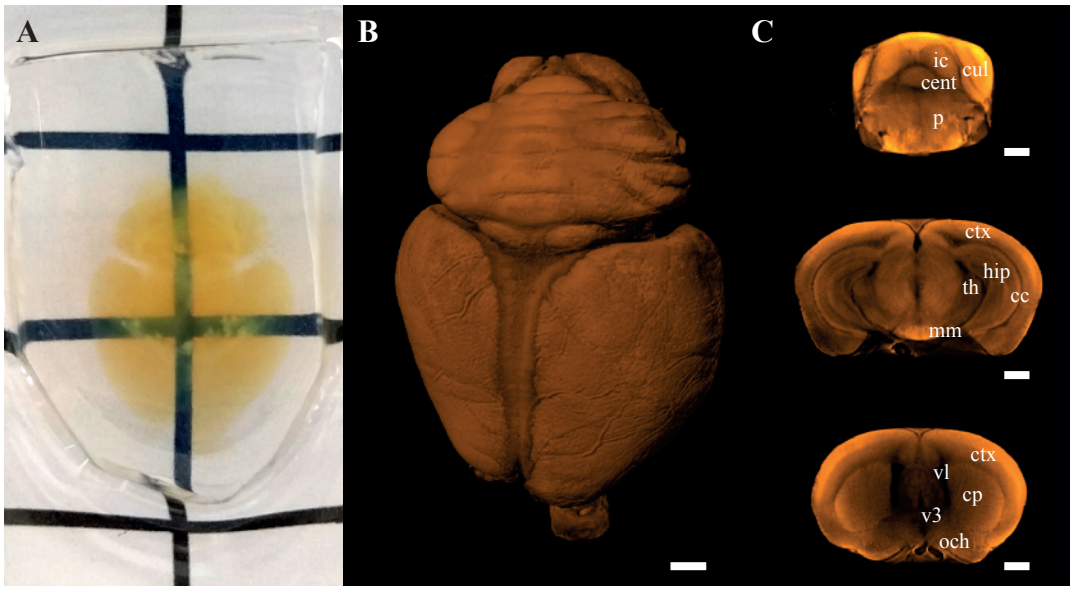

Fig. 3. Photograph of a mounted and cleared 8-month-old B6SJL F1 mouse brain (A). 3D rendering of the OPT image obtained from tissue autofluorescence (B, Visualization 1). Single coronal sections of the OPT image (C) showing the inner morphology of the intact organ: cc, corpus callosum; cent, central lobule; cp, caudoputamen; ctx, cerebral cortex; cul, culmen; hip, hippocampal region; ic, inferior colliculus; mm, medial mammillary nucleus; och, optic chiasm; p, pons; th, thalamus; v3, third ventricle; vl, lateral ventricle. Grid spacing (in A): 1 cm. Scale bars: 1 mm.

3.2. *Vascular network*

Vascular abnormalities play an important role in cognitive decline and inflammation in some AD patients. To demonstrate the compatibility of our clearing protocol with a fluorescence labeling of the vasculature, we perfused the animals with an FITC-albumin hydrogel. This labeling method was performed on 4-month-old B6SJL F1 mouse brains (n=2) and the resulting images, acquired using the OPT system with the 470-nm excitation illumination, are shown in Fig. 4. In this configuration, we can identify a variety of vascular compartments, including the superior sagittal sinus (SSS) and the sigmoid sinus (SS), which are venous sinuses found within the dura mater, the outermost layer surrounding the central nervous system, and located on top of the brain (Fig. 4(A)). The caudal rhinal vein (CRV), running on the side of the brain in a sagittal manner (Fig. 4(B)), the anterior cerebral artery (ACA), which partly forms the circle of Willis, ring-shaped system of arteries, situated at the base of the brain (Fig. 4(C)), and the middle cerebral artery (MCA) traveling from the circle of Willis to the top of the brain. To better appreciate the 3D nature of the blood vessels, we created maximum intensity projections from 20 consecutive OPT sections at different positions of the brain (Fig. 4(D)). These artificial sections

Biomedical Optics EXPRESS

represent half a millimeter of the whole brain sliced coronally and highlight penetrating vessels several millimeters in depth. However, smaller vessels, such as capillaries, have a diameter of typically less than 10 μm and fall beyond our resolution limit. The innermost vessels of the brains are seemingly undetected. This could be due to the depletion of the fluorescence signal propagating through the sample as well as the shadowing from the surface vasculature. Ultimately, the identification of large brain vessels with the hydrogel perfusion extends the phenotyping capacity of OPT and has potential application in the study of aneurysms, strokes, and vascular development [40].

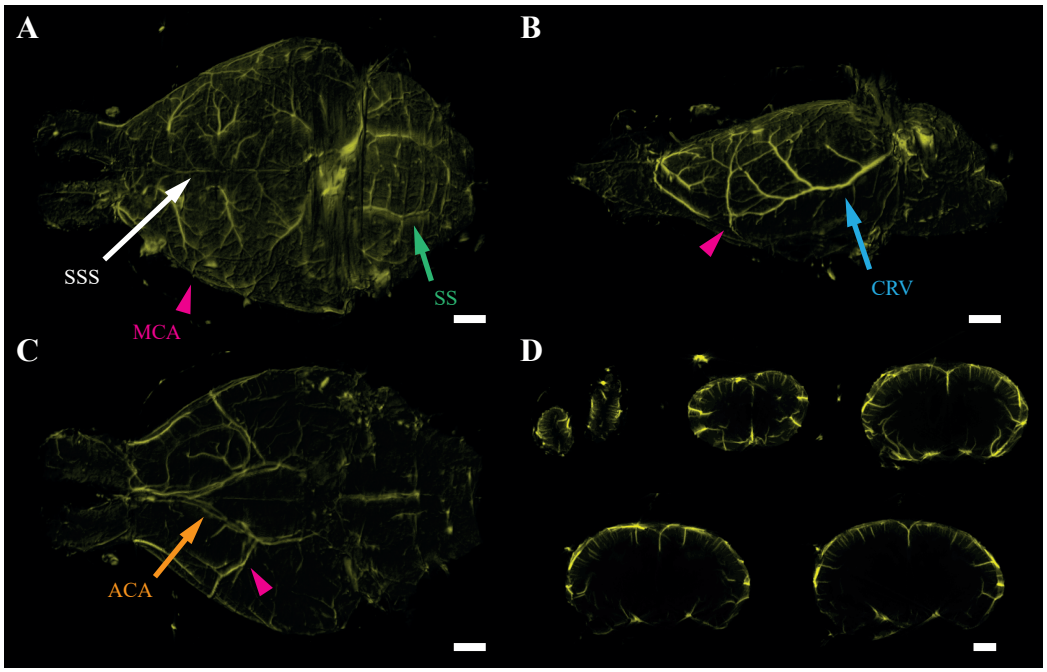

Fig. 4. Visualization of the brain vasculature in a 4-month-old B6SJL F1 mouse. The brain was perfused with an FITC-albumin hydrogel and imaged with OPT. 3D rendering from the top (A), side (B), and bottom (C) view (see Visualization 2). Maximum intensity projections of 20 coronal sections through the whole brain (D) showing the penetrating venules/arterioles. ACA, anterior cerebral artery; CRV, caudal rhinal vein; MCA, middle cerebral artery; SS, sigmoid sinus; SSS, superior sagittal sinus. Scale bars: 1 mm.

3.3. *Amyloid deposition*

New amyloid imaging agents, based on the chemical structure of histologic dyes, are now making it possible to track amyloid pathology along with disease progression. To show the compatibility of our clearing protocol with fluorescence labeling of amyloid deposits, we injected the animals IP with an amyloid-binding dye called Methoxy-X04. This labeling method was performed on 8-month-old 5xFAD mouse brains (n=3) and the resulting images, acquired using the OPT system with the 420-nm excitation illumination, are shown in Fig. 5. Individual sections of the three-dimensional OPT image (Fig. 5(A)) reveal a mixed contrast between the brain anatomy and amyloid plaques, seen as bright dot agglomerates (denser zones pointed out by the arrows), caused by the overlap of the autofluorescence and the Methoxy-X04 emission spectra. The 3D rendering of the whole brain, presented in Fig. 5(B), reveals the amyloid distribution in the organ and highlight an important aggregation in the subiculum (Fig. 5(B) and 5(C)). This result adds to

Biomedical Optics EXPRESS

the findings of Oakley *et al.* [35], who used histology to localize amyloid deposition, providing deeper insights into the 3D distribution of the amyloid plaques. Interestingly, the pathological phenotype observed in the 5xFAD mice shows differences in the 3D distribution compared to the APPPS1 model used in the work of Jährling *et al.* [11] at a comparable age. This observation further demonstrates the high potential of OPT for fast phenotyping. Small plaques (below 50 µm) are blurred out due to the system's resolution.

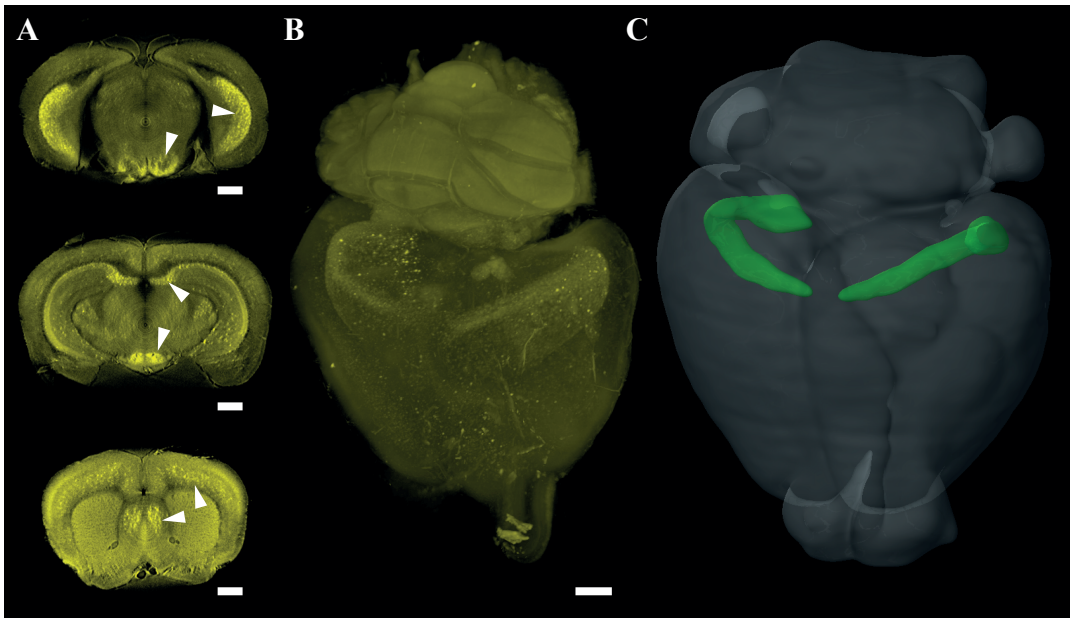

Fig. 5. 3D imaging of amyloid deposition in an 8-month-old 5xFAD mouse. Single coronal sections (A) with the arrows pointing to regions with high deposition and three-dimensional rendering of the OPT image (B, Visualization 3). A 3D image of the subiculum (green) is shown within a whole mouse brain (C) to compare with the location of amyloid deposition. Image (C) was obtained from the Allen mouse brain atlas [41]. Scale bars: 1 mm.

3.4. Histology comparison

The proposed framework for rapid mouse brain imaging with OPT extends the current 3D capability of traditional histology. For this reason, we performed a qualitative comparison of both techniques by splitting labeled mouse brains into hemispheres. The hemispheres were then processed separately: one was prepared for histology (Fig. 6(A) and 6(D)), and the other one for OPT (Fig. 6(B)-(C) and 6(E)).

First, the result of this comparison for the vasculature in a 9-month-old B6SJL F1 mouse brain is shown in Fig. 6(A)-(C). The histological slice (Fig. 6(A), Visualization 4) displays details of the microvasculature as well as larger vessels, pointed by pink arrows. However, the acquisition and stitching of the images took almost an hour for a single section. Additionally, stitching artifacts, such as the one pointed by the blue arrow, remain visible in the figure. On the other hand, some of the large vessels (pink arrows) can be identified in the OPT section (Fig. 6(B)), but the microvasculature is not resolved. Additionally, we used the 3D capability of OPT to produce a maximum intensity projection (Fig. 6(C)) from 20 consecutive sections (approx. 0.5 mm in thickness), which reveals a range of penetrating vessels otherwise difficult to obtain in histology.

Second, the result of the comparison for the amyloid plaques in a 3-month-old 5xFAD mouse brain is shown in Fig. 6(D)-(E). The histological slice (Fig. 6(D), Visualization 5) present a

Biomedical Optics EXPRESS

high-resolution mixed contrast between tissue autofluorescence and amyloid plaques (regions of accumulation pointed by green arrows). However, the acquisition and stitching took approximately an hour, and the resulting section suffers from microtome artifacts (blue arrows). On the other hand, the regions of plaques accumulation (green arrows) could be retrieved in the OPT section (Fig. 6(E)) with a lower resolution. Additionally, we observed an opposed contrast in some regions of the brain, such as the corpus callosum (cc), which is bright in the histological section but appears dark in OPT. This might be caused by the chemical clearing.

These results highlight the complementarity of traditional histology and OPT. Mechanical slicing associated with wide-field fluorescence microscopy produces high-resolution images of the features of interest in 2D. However, this method can be cumbersome (particularly the cutting and stitching parts) and is hardly suitable for 3D imaging. On the other hand, OPT produces low-resolution 3D images of the whole organ in about 5 minutes with a user-friendly sample preparation.

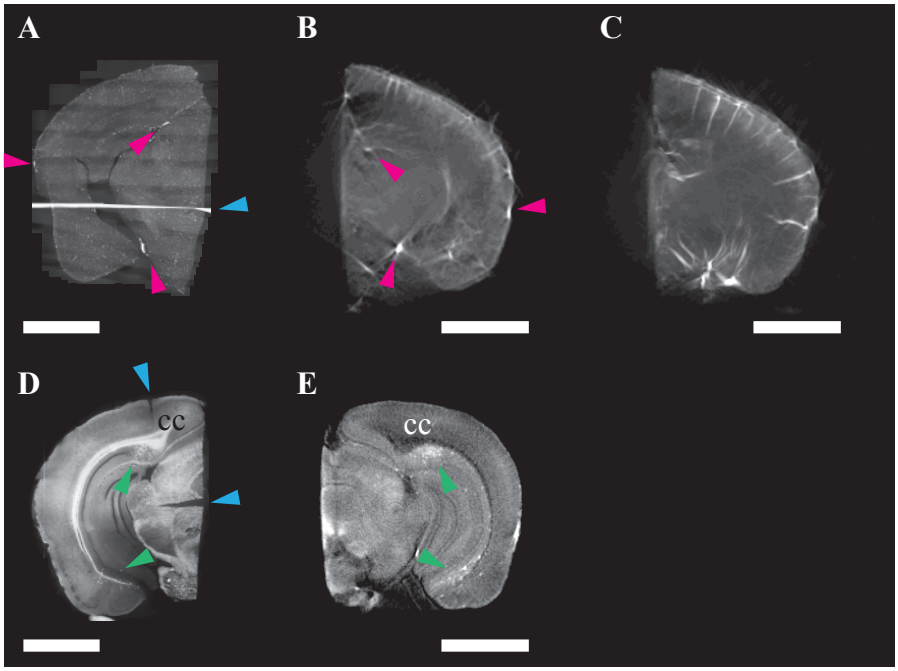

Fig. 6. Comparison of histological and OPT slices. 40 µm-coronal section of a 9-month-old B6SJL F1 mouse brain hemisphere labeled for vasculature (A, Visualization 4) and corresponding single OPT section (B). A maximum intensity projection (C) taken over 20 consecutive OPT sections, which represents approximately 0.5 mm in thickness, gives a better representation of the penetrating vessels and highlights the 3D advantage of this technique. 40 µm-coronal section of a 3-month-old 5xFAD mouse brain hemisphere labeled for plaques (D, Visualization 5) and corresponding single OPT section (E), some regions such as the corpus callosum (cc) show an inverted contrast. Scale bars: 2 mm.

4. Conclusion

In this manuscript, we present a novel OPT method for whole mouse brain imaging. This method is based on a custom OPT system, designed for mouse brain imaging, and an optimized sample preparation. The OPT system provides an FOV of 26.6 x 26.6 mm^2 and can image samples as thick as 26 mm typically within less than 5 minutes. It incorporates an epifluorescence arm,

Biomedical Optics EXPRESS

which provides a uniform full-field illumination and is easily configurable by switching the excitation LEDs and filters. The sample preparation consists of a simple and rapid solvent-based clearing of the organ (3 changes of clearing solution in 3 days). This can be complemented with fluorescence labeling of the vasculature, through perfusion of a fluorescent hydrogel, or labeling of amyloid deposition in a mouse model of AD, via 2 consecutive injections of an amyloid-binding dye. Based on this method, we imaged B6SJL F1 mouse brains without markers. The results demonstrate the quality of the clearing and reveal details of the organ structure, an essential requirement of neuroanatomical phenotyping [33]. Additionally, by imaging the vasculature of B6SJL F1 mouse brains, we identify major vessels, as well as penetrating arterioles/venules in 3D down to several millimeters in depth. We also imaged 5xFAD mouse brains with labeled amyloid deposition. Individual sections of the OPT image revealed regions of accumulated amyloid plaques. Through 3D rendering, we could identify the subiculum as the region with the densest accumulation, in concordance with the literature [35]. Finally, we performed a qualitative comparison of histological and OPT slices in the different hemispheres of the same brain to illustrate the complementarity of these two techniques.

The rapid acquisition of whole mouse brains with our OPT system is achieved through a long DOF and a low magnification, which currently limit the resolution to ~50 µm. Additionally, the low NA of the system restricts the light collection efficiency. This would be a plausible explanation for why finer structures such as capillaries and small amyloid plaques (<50 µm) were undetectable. Furthermore, the method requires embedding of the sample in agarose for mounting purposes. While the surrounding agarose simplifies the clearing protocol, by creating an interface with the solvents and avoiding the use of increasing concentration solutions, it has not been tested yet with other clearing methods such as CLARITY [42], SeeDB [39], Sca*l*e [43], or 3DISCO [44].

In the future, other clearing methods optimized for OPT might improve the current results obtained with BABB; new amyloid imaging agents with a distinct excitation/emission spectrum will help to discriminate between the tissue autofluorescence and the amyloid plaques. Additionally, our imaging method shows high potential for the use in neuropathology and the study of disease progression, similarly to the work and research in diabetes [30, 31], by imaging the mouse pancreas at different ages. Ultimately, our OPT setup with its large FOV is well suited for the imaging of other organs, such as the liver, lung, and kidney.

Supporting information

The 3D reconstructed OPT datasets used to generate Fig. 3-5 can be downloaded from our website at https://lob.epfl.ch/files/content/sites/lob/files/shared/downloads/brainOPT.zip/.

Funding

The authors greatly acknowledge the funding from: EU Framework Programme for Research and Innovation (602812, 686271); Commission for Technology and Innovation (CTI) (13964.1, 17537.2); Lundbergs Foundation (2014/2073); Novo Nordisk Foundation (NNF150C0016146); Royal Physiographic Society.

Acknowledgments

The authors would like to thank Amélie C. M.-O. Ducrey and Silas Schlatter for their helpful contributions during their semester projects.

The authors would also like to show their gratitude to the Histology Core Facility (HCF) of EPFL for the slicing and mounting of the brain hemispheres with the microtome.

Biomedical Optics EXPRESS

Disclosures

The authors declare that there are no conflicts of interest related to this article.